JACS
JOURNAL OF THE AMERICAN CHEMICAL SOCIETY

ARTICLE

pubs.acs.org/JACS

Gelification: An Effective Measure for Achieving Differently Sized Biocompatible Fe_3O_4 Nanocrystals through a Single Preparation Recipe

Qiaojuan Jia,[†] Jianfeng Zeng,[†] Ruirui Qiao,[†] Lihong Jing,[†] Liang Peng,[‡] Fenglong Gu,[*,‡] and Mingyuan Gao[*,†]

[†]Institute of Chemistry, The Chinese Academy of Sciences, Bei Yi Jie 2, Zhong Guan Cun, Beijing 100190, China

[‡]Center for Computational Quantum Chemistry, South China Normal University, Guangzhou 510631, China

Supporting Information

ABSTRACT: Biocompatible Fe_3O_4 nanocrystals were synthesized through the pyrolysis of ferric acetylacetonate ($Fe(acac)_3$) in diphenyl oxide, in the presence of α,ω-dicarboxyl-terminated polyethylene glycol (HOOC−PEG−COOH) and oleylamine. Unusual gelification phenomena were observed from the aliquots extracted at different reaction stages after they were cooled to room temperature. By reaction time, the average size of the Fe_3O_4 nanocrystals was tuned from 5.8 to 11.7 nm with an equilibrium size around 11.3 nm. By increasing the gelification degree of the stock solution, the equilibrium size of the Fe_3O_4 nanocrystals was further increased from 11.3 to 18.9 nm. The underlying gel formation mechanism was investigated by using ultraviolet−visible absorption spectroscopy and Fourier transform infrared spectroscopy. The results suggest that the complexation between HOOC−PEG−COOH and $Fe(acac)_3$, with the help of oleylamine, results in large molecular networks, which are responsible for the gelification of the stock solution, while the interaction between the fragment of the molecular network and Fe_3O_4 nanocrystal is responsible for the second gelification process observed during the early stage of reflux. To further investigate the particle growth behavior, small molecules released during the preparation were collected and analyzed by using photoelectron spectroscopy/photoionization mass spectroscopy (PES/PIMS). It was demonstrated that the pyrolysis of the Fe precursor is strongly correlated with the particle growth process. Further numerical simulations reveal that the first gelification process induced by the complexation between HOOC−PEG−COOH and $Fe(acac)_3$ largely alters the pyrolysis behavior of the Fe precursor; consequently, the equilibrium size of the resultant Fe_3O_4 nanocrystals can effectively be tuned by the gelification degree of the stock solution.

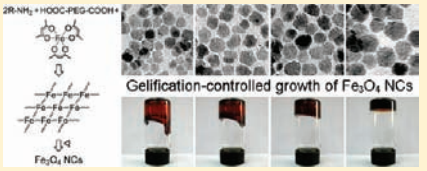

INTRODUCTION

Because of the quantum confinement effect and the nanometer size effect, inorganic nanocrystals exhibit unique particle size-dependent physical properties.[1,2] Although great success has been achieved over the past decades in regulating the particle size of various types of inorganic nanocrystals synthesized through different synthetic principles,[3−9] developing new synthetic routes and further exploring the mechanisms for delicate control over the particle size remain hot subjects for wet-chemical synthesis of inorganic nanocrystals, especially for magnetic iron oxide nanocrystals due to their bright future in nanomedicine.

The pioneering work of Alivisatos' group on γ-Fe_2O_3 nanocrystals, prepared by pyrolyzing metal Cupferron complexes $Fe(Cup)_3$ (Cup: *N*-nitrosophenylhydroxylamine) at 200−300 °C via a "hot-injection" method (i.e., a stock solution of the metal precursor is quickly injected into a hot solvent), has paved a new synthetic route for high-quality magnetic iron oxide nanocrystals.[10] Hyeon and co-workers developed the above-mentioned synthesis by using $Fe(CO)_5$ instead of metal Cupferron complexes in producing monodispersed γ-Fe_2O_3 nanocrystals.[11] By varying the molar ratio of $Fe(CO)_5$ to oleic acid, which serves as stabilizing agent, the size of the resultant nanocrystals was tuned in a range of 4−11 nm. Via a seed-mediated growth, larger γ-Fe_2O_3 nanocrystals (16 nm) were obtained.[11,12] Sun and co-workers for the first time reported the synthesis of highly monodispersed Fe_3O_4 nanocrystals by pyrolyzing iron(III) acetylacetonate ($Fe(acac)_3$) in the presence of oleic acid, oleylamine, and 1,2-hexadecanediol in 2002.[7] Most importantly, a "heating-up" method (i.e., heating the solution consisting of all reactants to designed temperatures) was introduced and adopted instead of the "hot-injection" method, although the latter approach was believed to be reasonable and effective for achieving monodispersed nanocrystals through the burst of nucleation followed solely by the particle growth process. The as-prepared nanocrystal was typically around 4−6 nm. Via the seed-mediated growth, a larger Fe_3O_4 nanocrystal of 20 nm was obtained.[13] Upon a similar approach, a series of 3−20 nm metal-doped iron oxide of spinel MFe_2O_4 (M = Mn, Fe, Co) nanocrystals were synthesized.[13] Following the "heating-up" method, Peng and co-workers reported a simple, reproducible, and general method for preparing monodispersed metal oxide nanocrystals by pyrolyzing metal−fatty acid salts.[14] They also found that the amount and chain length of the fatty acid, serving as the particle surface capping

Received: August 29, 2011
Published: October 27, 2011

agent, exerted strong effects in regulating the size of the resultant Fe_3O_4 nanocrystals. Under optimized conditions, monodispersed magnetic iron oxide nanocrystals of 6−30 nm were obtained.[14] Moreover, they further demonstrated that the use of excessive fatty acid was in favor of larger particles, while the presence of amines and alcohols as activating reagents led to smaller particles of 3−4 nm. This synthetic approach was used for producing monodispersed $(\gamma\text{-}Fe_2O_3)_{1-x}(Fe_3O_4)_x$ nanocrystals at an ultra-large-scale (tens of grams) by Hyeon and co-workers.[6] They also reported differently sized iron oxide nanocrystals synthesized by using organic solvents with different boiling points (bp), for example, 5 nm in 1-hexdecane (bp, 274 °C), 9 nm in octyl ether (bp, 287 °C), 12 nm in 1-octadecene (bp, 317 °C), 16 nm in 1-eicosene (bp, 330 °C), and 22 nm in trioctylamine (bp, 365 °C), and found that x increased against the reaction temperature.[6] Nevertheless, the alternation of the solvent may also introduce additional solvent effects apart from simply varying the reaction temperature. For example, Alivisatos and co-workers observed that higher reaction temperature was in favor of smaller $\gamma\text{-}Fe_2O_3$ nanocrystals prepared through the "hot-injection" of $Fe(CO)_5$ into octyl ether.[15] It is generally easier to understand the latter case as higher reaction temperature speeds up the pyrolysis of metal precursors, which is in favor of the formation of nuclei with higher concentrations.

In brief, the aforementioned investigations have demonstrated that the reaction temperature,[6,13,15] the concentration and the chemical nature of the precursor,[16,17] the surface capping agent and its ratio to precursor,[14,18,19] etc., play important roles in regulating the size of the resultant iron oxide nanocrystals. This is because the reaction temperature, the chemical nature, and the concentration of the precursor are directly associated with the supplying rate and the resultant concentration of the monomer in forming the target nanocrystals. Meanwhile, the surface capping agents, used for stopping the growth of the resultant nanocrystals by firmly anchoring on the particle surface, also play an important role in the particle size regulation. In addition, some surface capping agents such as alkylamines also exhibit strong particle size-regulation ability as they were believed to catalyze the pyrolysis of some iron−organic precursors.[13,14,20]

Although there are so many parameters practically used for regulating the size of iron oxide nanocrystals, the growth of a colloidal particle is generally believed to be strongly associated with the diffusion of monomer to the surface of nuclei and the following surface reaction of monomer with nuclei. Therefore, two different growth models associated with these two processes are proposed on the basis of classic kinetics theory and widely adopted for interpreting the growth behavior of inorganic colloidal particles in solution, that is, the diffusion-controlled growth model and reaction-controlled growth model.[21−24] The diffusion-controlled model postulates that the particle growth rate depends on the flux of the monomers supplied to the particles,[25−27] whereas the reaction-controlled growth model takes the precipitation and dissolution of monomers into consideration.[22,23,28] Nevertheless, the growth of nanocrystals prepared through the thermal decomposition of metal−organic precursors is too complicated to be simply depicted by these two growth models. Recently, an important breakthrough has been achieved by Bawendi and co-workers in developing a kinetic model for describing the nanocrystal nucleation and growth by taking the chemical conversion of precursors to monomers into consideration.[29] Two nondimensional parameters were extracted and successfully applied for describing the nanocrystal nucleation and growth behaviors in various thermal decomposition systems for predicting the effects of the experimental conditions on both nanocrystal size and size distribution.[29]

However, the nucleation and growth of iron oxide nanocrystals produced by the thermal decomposition method upon the uses of various types of metal−organic precursors are still important subjects of further investigations, due to the lack of enough knowledge on the corresponding pyrolysis reactions with the particle ligands being deeply involved. In other words, the impact of the complexation reaction between the surface capping molecules and the metal ions from the precursors on the growth kinetics of the resultant nanocrystals is far from clear. Recently, an unusual gelification of a $Cu(acac)_2/In(acac)_3$-in-dodecanethiol system, as an indicator of the formation of supramolecular structure between the particle ligand and the metal ions, was reported and demonstrated to have a strong impact on the growth of the resultant Cu−In−S nanocrystals formed through successive pyrolysis of $Cu(acac)_2$ and $In(acac)_3$ precursors.[30]

Following our previous investigations on water-soluble and biocompatible Fe_3O_4 nanocrystals prepared by pyrolyzing $Fe(acac)_3$ in various types of high boiling point solvents,[31−38] herein we report our recent investigations on the gelification-associated size regulation effect for biocompatible Fe_3O_4 nanocrystals produced by pyrolyzing $Fe(acac)_3$ in diphenyl oxide in the presence of α,ω-dicarboxyl-terminated polyethylene glycol (HOOC−PEG−COOH) and oleylamine. The PEG-coated Fe_3O_4 nanocrystals ranging from 5.8 to 18.9 nm were obtained through a single preparation recipe simply by varying the reaction time and the gelification degree of the stock solution. The underlying gel formation mechanism was investigated. The gelification-associated size regulation effect was discussed in combination with the numerical simulation based on the theoretical method recently reported by Bawendi and co-workers.[29]

EXPERIMENTAL SECTION

Chemicals. Iron(III) acetylacetonate ($Fe(acac)_3$) was purchased from Aldrich (14024-18-1, 97%) and used after twice recrystallization. Diphenyl oxide (bp, 259 °C) was used after vacuum distillation. HOOC−PEG−COOH (M_n = 2000) was synthesized according to a previous report.[33] Oleylamine was purchased from Fluka (112-90-3, ≥70%) and used as received. Other chemicals of analytical grade including ethanol, dichloromethane, and ether were used as received.

Synthesis of Fe_3O_4 Nanocrystals. Typically, 2.12 g (6 mmol) of $Fe(acac)_3$, 7.90 mL (24 mmol) of oleylamine, and 24.0 g (12 mmol) of HOOC−PEG−COOH were dissolved in 100 mL of diphenyl oxide solution. After being purged with nitrogen for 2 h, the solution was heated to reflux within 15 min. Under mechanical stirring at 400 rpm, different aliquots were extracted during the heating process before and after the reaction mixture got refluxed for monitoring the particle formation and growth. Upon addition of a mixture of ethanol and ether (vol:vol = 1:5) into the aliquots at room temperature, the resultant nanocrystals were precipitated and isolated. By being redispersed in ethanol and subsequently precipitated with ether for three cycles, the nanocrystals were purified and collected for further characterizations.

Conversion Rate of Fe_3O_4 Nanocrystals. The conversion rate of the decomposition reaction leading to iron oxide nanocrystals was defined herein as $[Fe]_{iron\ oxide}/[Fe]_{reactant}$, where $[Fe]_{iron\ oxide}$ stands for the concentration of Fe derived from the iron oxide particles in each aliquot and $[Fe]_{reactant}$ corresponds to the feeding concentration of $Fe(acac)_3$. $[Fe]_{iron\ oxide}$ was experimentally determined by the 1,10-phenanthroline spectrophotometric method and inductively coupled

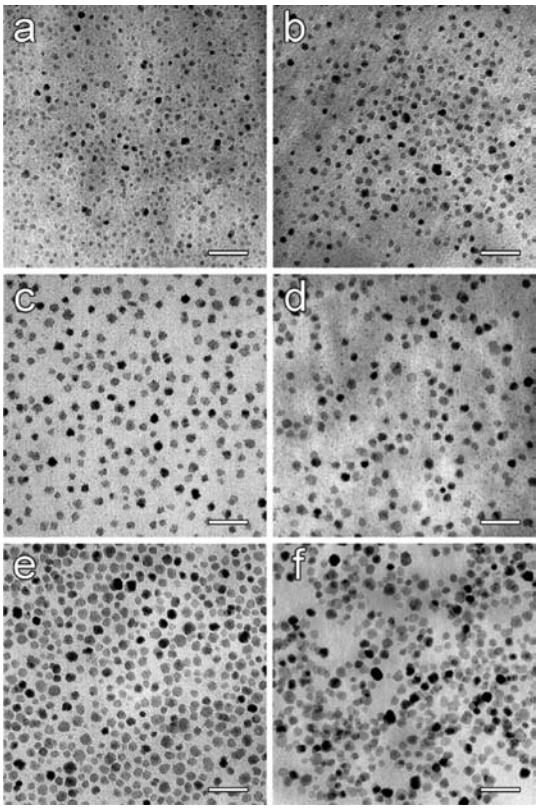

Figure 1. TEM images of Fe_3O_4 nanocrystals obtained by reflux time of 0 min (a), 10 min (b), 15 min (c), 20 min (d), 30 min (e), and 60 min (f), respectively. The scale bars correspond to 50 nm.

plasma atomic emission spectroscopy (ICP-AES) after the resultant nanocrystals were digested by HCl.

Characterizations. Transmission electron microscope (TEM) images of the nanocrystals were taken on a JEM-100CXII electron microscope at an acceleration voltage of 100 kV. The particle size was determined by counting more than 400 nanocrystals per sample. Powder X-ray diffraction (XRD) pattern of the particle samples was recorded on a Regaku D/Max-2500 diffractometer under Cu Kα_1 radiation (λ = 1.54056 Å). TGA measurements were performed on a NETZSCH TG209F3 thermogravimetric analyzer. The magnetic properties of the resultant samples were characterized by using a vibrating sample magnetometer (VSM JDM-13, China). Dynamic light scattering (DLS) measurements were carried out at 298.0 K with a Nano ZS (Malvern) equipped with a solid-state He−Ne laser (λ = 633 nm) for measuring the hydrodynamic size of the resultant nanoparticles. Fourier transform infrared (FTIR) spectra and UV−Vis absorption spectra of the reaction mixtures with different combinations of reactants were recorded at room temperature on a Bruker EQUINOX55 FT-IR spectrometer and a Cary 50 UV−Vis absorption spectrometer, respectively. The shear viscosity of the stock solutions after being aged at controlled temperature for different periods of time was measured on a TA AR2000 stress-controlled rheometer equipped with two parallel plates of 40 mm in diameter at 30 °C. The concentration of Fe was determined by using an inductively coupled plasma atomic emission spectrometer (ICP-2000) produced by Jiangsu Skyray Instrument Co., Ltd. The photoelectron spectroscopy/photoionization mass spectroscopy (PES/PIMS) measurements on small molecules released during the preparation were carried out on a homemade setup.[39] The PES resolution of the HeI photoelectron spectrometer equipped was of about 30 meV, and the PIMS resolution was of 410 at m/z = 254.

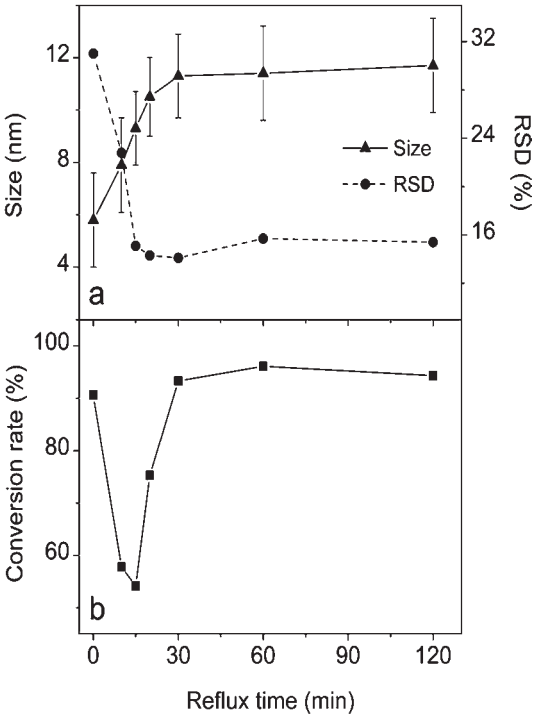

Figure 2. Frame a: Temporal evolutions of the particle size and size distribution. Frame b: The conversion rate of Fe_3O_4 nanocrystals against reflux time.

RESULTS

Size Evolution, Crystalline Structure, and Magnetic Properties of the As-Prepared Nanoparticles. The TEM images of the as-prepared nanoparticles obtained by reflux time of 0 min (right after the reaction system got refluxed at 253 °C), 10 min, 15 min, 20 min, 30 min, and 60 min are shown in Figure 1. In general, the particle size quickly increases against the reflux time within the initial 30 min of reflux and then becomes nearly unchanged upon prolonged reflux as shown in Figure 2a. It should be mentioned that in all preparation systems containing HOOC−PEG−COOH reported herein, irrespective of the aging process purposely implemented for increasing the gelification degree of the stock solutions as discussed below, the nanoparticles were found to finish the fast growing process within 30 min. Therefore, the average particle size achieved at 30 min of reflux was defined as the equilibrium size of the nanoparticles even though prolonged reflux can slightly increase the particle size. Along with the particle growth, the particle size distribution, defined by the relative standard deviation (RSD) of the particle size, dramatically decreases and then slightly increases after the particle growth is slowed down. The conversion rate of iron oxide nanoparticles shown in Figure 2b, however, presents a nonmonotonic behavior comprised of three distinct regions. During the first 15 min of reflux, it dramatically decreases to a minimum of 54.2% and then quickly increases to 93.3% at 30 min of reflux. After that, it slowly increases to ~95% upon prolonged reflux. The unexpected decrease presented within the initial 15 min of reflux will be discussed in the following section. Yet by comparing the quick increase with the particle growth tendency, it can be concluded that the following conversion rate of Fe_3O_4 is mainly contributed by the particle growth.

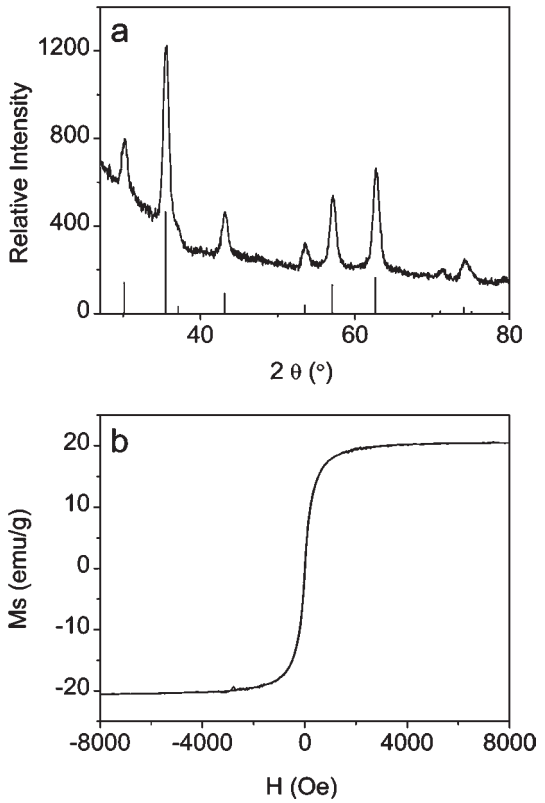

Figure 3. Frame a: Powder X-ray diffraction pattern of the particles shown in Figure 1e together with the JCPDS card (86-0866) data for magnetite shown at the bottom. Frame b: Room-temperature magnetization curve of the corresponding Fe_3O_4 nanocrystal sample.

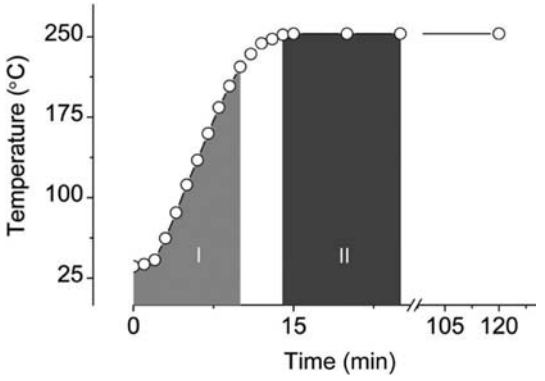

Figure 4. The temperature-rising curve of the reaction system for producing the nanoparticles shown in Figure 1. The light gray and dark gray regions shadow the temperature points at which the aliquots extracted became gels at room temperature.

Because the nanoparticles nearly stop growing in size after 30 min of reflux, the resultant nanoparticles extracted at 30 min of reflux were subjected to further characterizations. The powder XRD results shown in Figure 3a suggest that the resultant nanoparticles are Fe_3O_4 nanocrystals, which is also supported by the fact that the Fe^{3+}:Fe^{2+} ratio in the resultant nanocrystals was of 2:1 determined by the phenanthroline spectrophotometric method. According to the diffraction peak of (311), the average nanocrystal size was calculated to be 11.1 nm by the Scherrer formula, quite well in consistence with the TEM size.

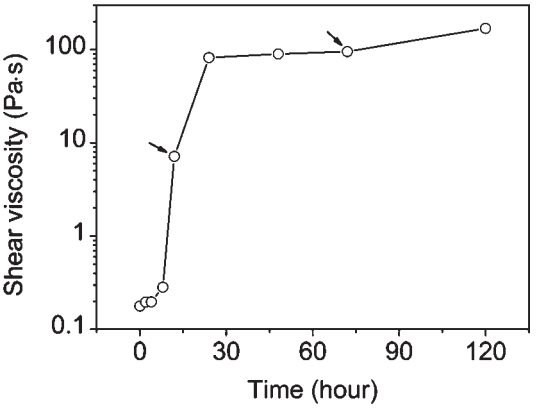

Figure 5. The shear viscosity of the stock solutions obtained after being aged at 40 °C for different periods of time. The arrows point to the incubated mixtures used for the following preparations.

The magnetic property of the nanocrystals was investigated by using a vibrating sample magnetometer (VSM). The room-temperature magnetization curve shown in Figure 3b suggests that the nanocrystals are superparamagnetic with a saturation magnetization of 20.5 emu/g. According to the TGA result shown in Figure S1 in the Supporting Information, the saturation magnetization of pure Fe_3O_4 nanocrystals is calculated to be around 50.2 emu/g. It should be mentioned that HOOC−PEG−COOH can in principle bridge the resultant nanoparticles forming particle aggregates. Nevertheless, under the current preparative conditions, as demonstrated by DLS results shown in Figure S2 in the Supporting Information, no particle aggregate was formed with respect to the particle samples shown in Figure 1.

Unusual Gelification Phenomena of the Reaction System. Quite unusual gelification phenomena were observed at room temperature from the aliquots extracted at different reaction stages. As a matter of fact, the stock solution already became sticky at room temperature during the deaeration process, which typically lasted for 2 h. The heating procedure further increased the viscosity of the reaction mixture until the reaction temperature reached 224 °C, which turned the aliquots extracted below 224 °C into gels at room temperature. Yet the following aliquots extracted before the reaction mixture got refluxed presented greatly reduced viscosity at room temperature. Quite unexpectedly, the aliquots extracted at 0 and 10 min of reflux became gels again at room temperature. Yet the gelification did not repeat with respect to the aliquots extracted later on. According to these experimental observations, the reaction mixture underwent two gelification processes showing increased viscosity as depicted in Figure 4. In fact, tiny nanoparticles were already formed, as shown in Figure S3 in the Supporting Information, at the end of the first gelification process at around 224 °C, which remains far below the refluxing temperature. It is therefore reasonable to believe that the gelification of the reaction system, as an indicator for the binding situations among reactants and intermediate species, should have a strong impact on the nucleation and the following growth of the Fe_3O_4 nanocrystals.[30]

Gelification-Associated Size Regulation Effect for Fe_3O_4 Nanocrystals. To further disclose the effects of gelification on the nucleation and growth of Fe_3O_4 nanocrystals, a series of stock solutions was prepared according to the recipe by which the nanocrystals shown in Figure 1 were prepared. They were then aged at designed temperatures for different periods of time

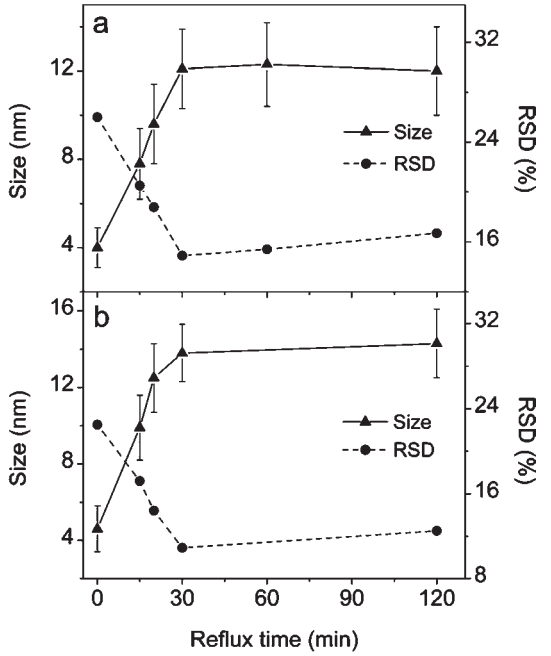

Figure 6. Temporal evolutions of the particle size and size distribution of the Fe_3O_4 nanocrystals prepared upon preaging the stock solution at 40 °C for 12 h (a) and 72 h (b), respectively.

before being used for preparing Fe_3O_4 nanocrystals under the same preparative conditions.

In detail, a series of identical stock solutions was prepared and then aged at 40 °C for different periods of time for monitoring the viscosity variation against the aging time. Offline viscosity measurements were carried out at a fixed shear rate of 10 s^{-1} at 30 °C, slightly above the freezing point of diphenyl oxide (27−28 °C). The shear viscosity results are shown in Figure 5. The viscosity first undergoes a quick increase over 2 orders of magnitude during the initial 24 h of aging. It remains nearly unchanged between 24 and 72 h of aging and then slightly increases again upon prolonged aging. On the basis of these results, two stock solutions aged at 40 °C by 12 and 72 h, respectively, were chosen for preparing Fe_3O_4 nanocrystals according to the procedures described in the Experimental Section. The reflux time-dependent particle size and size distribution of the resultant nanocrystals are shown in Figure 6. Similar to those shown in Figure 2, the nanocrystals obtained from these two systems also reach their equilibrium size at 30 min of reflux. Therefore, the nanocrystals prepared by 30 min of reflux were selected for further showing the gelification-associated size regulation effect.

The TEM results shown in Figure 7 reveal that 12 h of aging slightly increases the equilibrium size from 11.3 nm (Figure 1e) to 12.1 nm (Figure 7a), while 72 h of aging further increases it to 14.1 nm (Figure 7b). These results suggest that the equilibrium size of the resultant Fe_3O_4 nanocrystals is strongly dependent on the initial aging process. Following these results, two additional experiments were carried out by aging the stock solutions at higher temperatures, that is, 80 and 140 °C, respectively. It deserves to be mentioned that higher temperature greatly accelerated the gelification process. For example, at 80 °C, the viscosity of the stock solution quickly increased to the maximum value (112 Pa·s at 30 °C) within 2 h in contrast to 24 h required

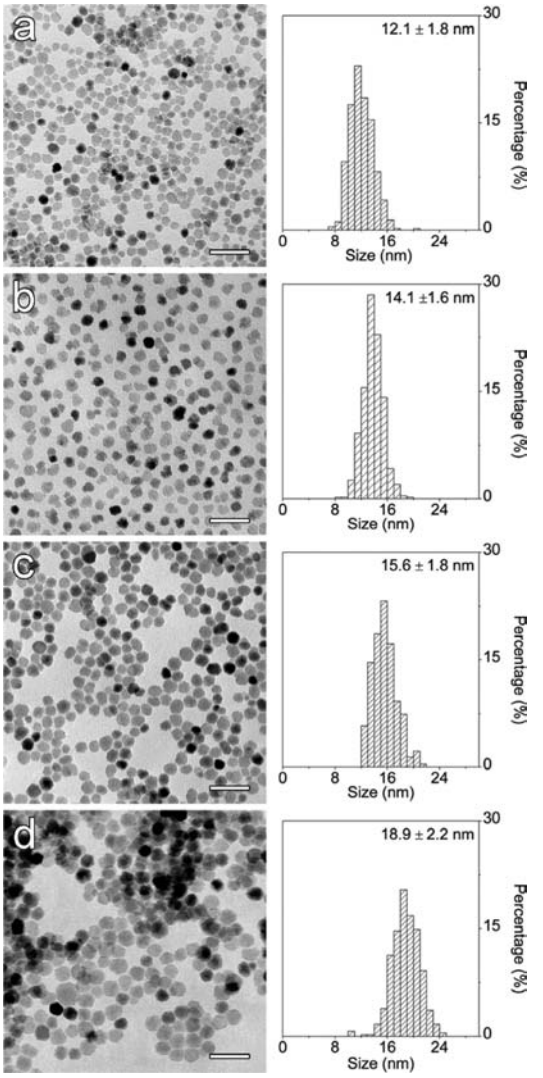

Figure 7. TEM images of the Fe_3O_4 nanocrystals prepared by aging the stock solutions with the same recipe at 40 °C for 12 h (a), at 40 °C for 72 h (b), at 80 °C for 4 h (c), and at 140 °C for 4 h (d), respectively, together with the histograms of the corresponding nanocrystals. All scale bars correspond to 50 nm.

at 40 °C and remained nearly unchanged during the following 24 h. According to these results, the aging time was set as 4 h for the stock solutions aged at 80 and 140 °C, respectively, prior to the reflux procedure. The Fe_3O_4 nanocrystals finally obtained are shown in Figure 7c and d. Statistical results reveal that 4 h of aging at 80 °C effectively increases the equilibrium size to 15.6 nm, while 4 h of aging at 140 °C further increases it to 18.9 nm.

■ DISCUSSION

As a matter of fact, the reaction temperature, precursor concentration, type of surface capping agents, and their ratio to metal precursors are commonly used synthetic parameters for regulating the size of magnetic iron oxide nanocrystals as well as many other types of inorganic nanocrystals. Yet gelification-associated effects on the growth of inorganic nanocrystals are rarely reported before. Typically, the surface capping agents required for the nanocrystal synthesis should have high enough binding affinity to metal element in the precursor. The

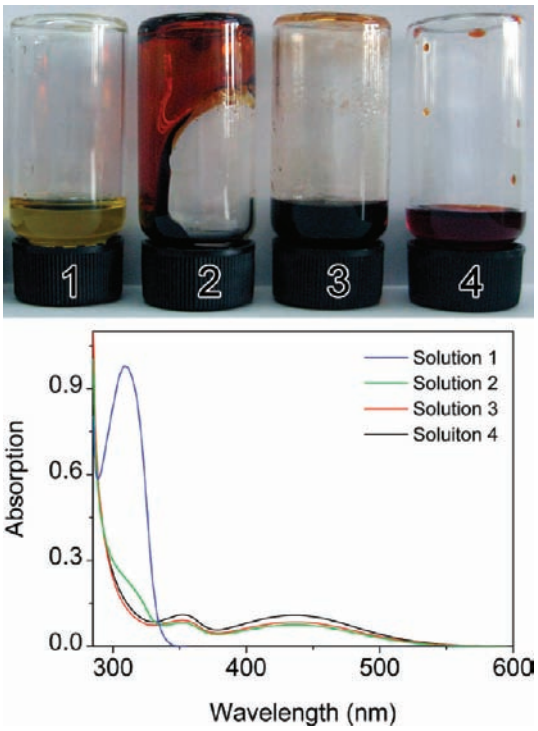

Figure 8. Top frame: Photographs of solution 1 (Hacac + HOOC−PEG−COOH + oleylamine), solution 2 ($Fe(acac)_3$ + HOOC−PEG−COOH + oleylamine), solution 3 ($Fe(acac)_3$ + HOOC−PEG−COOH), and solution 4 ($Fe(acac)_3$ + oleylamine). Bottom frame: The UV−Vis absorption spectra of these solutions. Note: The photographs were taken 5 h after they were prepared.

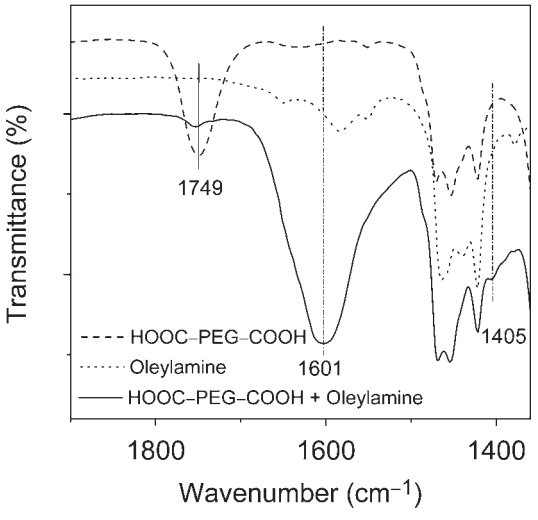

Figure 9. FTIR spectra of HOOC−PEG−COOH, oleylamine, and the mixture of HOOC−PEG−COOH and oleylamine in dichloromethane.

complexation between them sometimes leads to supramolecular structures of different forms, which under certain circumstances can immobilize the solvent molecules, leading to gelification of the reaction system.[30,40,41]

Gelification Mechanism of the Reaction System. The current synthetic system was comprised of $Fe(acac)_3$, HOOC−PEG−COOH, and oleylamine apart from diphenyl oxide serving as solvent. To disclose the gelification phenomena, solutions containing different combinations of the reactants, that is, Hacac (acetylacetone) + HOOC−PEG−COOH + oleylamine (solution 1), $Fe(acac)_3$ + HOOC−PEG−COOH + oleylamine (solution 2), $Fe(acac)_3$ + HOOC−PEG−COOH (solution 3), and $Fe(acac)_3$ + oleylamine (solution 4), were prepared to investigate the gel formation. The photographs shown in the upper frame of Figure 8 suggest that only when $Fe(acac)_3$, HOOC−PEG−COOH, and oleylamine are simultaneously present in diphenyl oxide does the gelification occur.

The UV−Vis absorption spectra of these solutions are shown in the lower frame of Figure 8 with those of $Fe(acac)_3$, oleylamine, and HOOC−PEG−COOH being provided in Figure S4. According to the literature, $Fe(acac)_3$ has two characteristic absorption bands at 351 and 434 nm corresponding to $d_\varepsilon \rightarrow \pi_4$ and $n \rightarrow d^*$ transitions, respectively,[42,43] while the characteristic absorption band of acetylacetone locates at around 274 nm.[44] Yet the latter band shifts to 309 nm in the spectrum of solution 1, probably due to the strong interaction of acetylacetone with HOOC−PEG−COOH and oleylamine. This absorption band appears as a shoulder in the spectrum of solution 2, which contains all of the reactants, but does not appear in the spectra of solutions 3 and 4, which suggests that acetylacetone is generated by replacing the ligands of $Fe(acac)_3$ upon the collective effort of HOOC−PEG−COOH and oleylamine. If HOOC−PEG−COOH forms a coordination bond with Fe with the help of oleylamine, the gelification can easily be understood because HOOC−PEG−COOH possessing two carboxyl groups at both ends meets the requirements for establishing a large molecular network together with multivalent metal ions. In contrast, the reaction system containing monocarboxylated PEG (M_n = 2000) instead of α,ω-dicarboxyl-terminated PEG did not exhibit gelification phenomena at all. More details will be described below.

To provide support for this hypothesis, FTIR investigations were performed. The typical IR spectra of HOOC−PEG−COOH, oleylamine, and their mixture in CH_2Cl_2 with a molar ratio of 1:2 are shown in Figure 9. It can be found that the C═O stretch band of carboxyl group, peaking at 1749 cm^{-1} in the spectrum of HOOC−PEG−COOH, disappears in the spectrum of the mixture of oleylamine and HOOC−PEG−COOH. Instead, two new absorption peaks appear at 1601 and 1405 cm^{-1}, which can be assigned to the $\upsilon_{as}(COO^-)$ and $\upsilon_s(COO^-)$ bands, respectively.[45] Therefore, it can be concluded that HOOC−PEG−COOH can form a primary amine salt with oleylamine by donating its proton, leading to the formation of $^-OOC-PEG-COO^-$, which then coordinates with $Fe(acac)_3$ by partly replacing the acetylacetonate ligand of $Fe(acac)_3$, because the binding constant of carboxylate group with Fe^{3+} (lg K_1 = 3.2) is quite comparable to the third step binding constant (lg k_3 = 4.6) for $Fe(acac)_3$.[46] According to these results, the gel formation mechanism for the first gelification process is proposed in Scheme 1. In brief, in the reaction system, the carboxylated PEG first reacts with oleylamine forming the primary amine salt, which subsequently coordinates with Fe atom in $Fe(acac)_3$ by partly replacing the acetylacetonate ligand, consequently leading to the formation of a large molecular network.

Because the thermal decomposition temperature for $Fe(acac)_3$ is around 189 °C,[47] and very small nanoparticles were observed at the end of the first gelification process at around 224 °C, it can therefore be deduced that the first gelification disappears while the molecular network partly breaks down for giving birth to the Fe_3O_4 nuclei. As the reactions go on, especially

Scheme 1. Schematic Drawing to Illustrate the First Gelification Process of the Reaction System Comprised of Fe(acac)$_3$, HOOC−PEG−COOH, and Oleylamine.

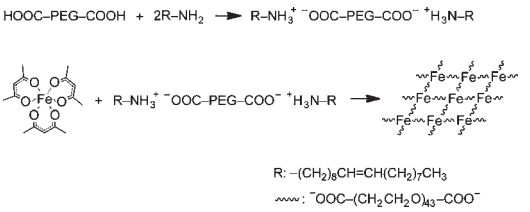

when Fe_3O_4 nanocrystals of 5.8−7.9 nm were formed during 0−10 min of reflux, corresponding to the second gelification process, the fragments of the polymeric network attaching on the nuclei surface effectively cross-link the nanoparticles again through the bivalent PEG to develop the second gelification process. Upon further decomposition of the network fragments serving as the precursor reservoir for the following particle growth, the second gelification disappears.

Thermal Decomposition of the Fe Precursors. The decomposition of metal precursors plays an important role in the nucleation and growth of nanocrystals.[17] Although Fe(acac)$_3$ served as Fe precursor in the current system, due to the formation of new coordination compounds between Fe(acac)$_3$ and HOOC−PEG−COOH, the decomposition of Fe precursor in the new forms becomes more complicated. The nucleation and growth kinetics of Fe_3O_4 nanocrystals are consequently altered as suggested by the experimental results shown in Figures 6 and 7 that the equilibrium size of Fe_3O_4 nanocrystals is strongly dependent on the gelification degree of the stock solution. To completely rule out the gelification-associated size regulation effect, two additional preparations were carried out.

In the first reaction system, HOOC−PEG−COOH was replaced by equal moles of mPEG−COOH with the rest of the contents in the recipe as well as the preparative procedures being kept unchanged. In such a system, no gelification phenomenon was observed, which supports that the bridging function of HOOC−PEG−COOH is crucial for the gelification of the reaction system. A series of aliquots was extracted during the reaction for monitoring the particle growth. The TEM images of four representative samples extracted at 0, 5, 10, and 20 min of reflux are shown in Figure 10. Different from the systems containing HOOC−PEG−COOH, a much smaller equilibrium size of 4.3−4.4 nm (Figure 10c and d) was reached within a shorter period of reflux, that is, 10 min. These differences suggest that the pyrolysis reactions can greatly be slowed by the complexation between HOOC−PEG−COOH and Fe(acac)$_3$ due to the introduction of higher energy barriers. Consequently, the supersaturation level as well as the number of nuclei are greatly reduced in the systems containing HOOC−PEG−COOH, which is in favor of the formation of larger nanocrystals.

In the second reaction system, only oleylamine was excluded. The gelification phenomenon was observed but only from the aliquots extracted after the reaction mixture got refluxed, which supports that small Fe_3O_4 particles are involved in the second gelification process as discussed above. The average size of the nanoparticles obtained after 2 h of reflux was only about 5.4 nm (Figure S5), suggesting that the second gelification process is much

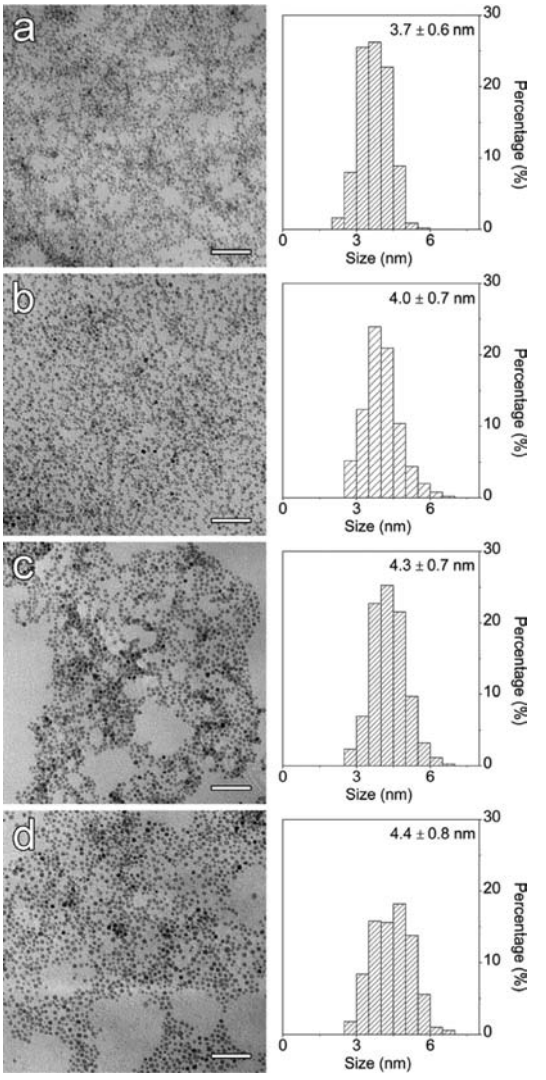

Figure 10. TEM images of the Fe_3O_4 nanocrystals extracted from the reaction mixture in which HOOC−PEG−COOH was replaced by equal moles of mPEG−COOH at reflux times of 0 min (a), 5 min (b), 10 min (c), and 20 min (d), respectively, together with the histograms of the corresponding nanocrystals. All scale bars correspond to 50 nm.

less effective in regulating the size of Fe_3O_4 nanocrystals in comparison with the first gelification process involving all reactants.

To get more information on the gelification-involved synthesis, photoelectron spectroscopy/photoionization mass spectroscopy (PES/PIMS) was used to analyze the small molecules released during the reaction. In brief, gaseous species released from the reaction solution were collected by passing through a U-shape glass tube immersed in liquid nitrogen in a Dewar flask, driven by a nitrogen stream. Next, upon slow addition of alcohol into the Dewar flask, the frozen gaseous species with different boiling points were released successively for the subsequent PES and PIMS measurements. The typical photoelectron spectra are shown in Figure S6. In brief, three types of small molecules were detected, that is, CO_2 (peaking at 13.78 and 18.08 eV), CH_3COCH_3 (peaking at 9.70 eV), and H_2O (peaking at 12.62 eV).[48]

To further correlate the generation of small molecules with the formation of Fe_3O_4 nanocrystals, the small molecules released at

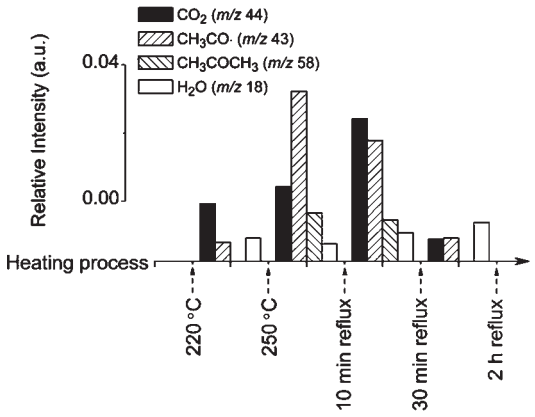

Figure 11. Photoionization MS signal intensities of the small molecules collected at different stages of the preparation.

different stages of the heating process were collected and then analyzed by photoionization mass spectroscopy. As small nanoparticles were observed when the reaction temperature reached 224 °C, five points along the heating process were set for collecting the small molecules released in between, that is, 220 °C, 250 °C, 10 min of reflux, 30 min of reflux, and 2 h of reflux at 253 °C. Four different types of signals were observed from the photoionization mass spectroscopy. The signals at $m/z = 44$ and 18 can be assigned to CO_2 and water, respectively, while the signals at $m/z = 53$ and 43 can be assigned to CH_3COCH_3 and its fragment $CH_3CO\cdot$, respectively. The evolutions of these signals are shown in Figure 11. According to previous investigations, acetone and CO_2 are the principal gaseous products for many acetylacetonates.[47,49,50] Therefore, the signal variations in acetone, $CH_3CO\cdot$, and CO_2 can be used for monitoring the pyrolysis reactions taking place in the current system. The CH_3COCH_3 fragment signal appears between 220 and 250 °C, and then reaches the maximum value during the second stage, that is, between 250 °C and 10 min of reflux at 253 °C. Although no CH_3COCH_3 signal was detected during the first stage, it also appears with the maximum value during the second stage. These results suggest that the degradation of Fe precursors already starts during the first observation stage, and then takes place more vigorously during the first 10 min of reflux. During the third stage, that is, 10−30 min of reflux, the signals of CH_3COCH_3 and $CH_3CO\cdot$ start to decrease and then the CH_3COCH_3 signal completely vanishes during the last stage, that is, 30 min to 2 h of reflux, which suggests that the acetone-related signals are strongly associated with the degradations of the Fe precursors in the new forms. In difference, the CO_2 signal appears during the first observation stage, but reaches the maximum value during the third stage where the particles grow dramatically in size. Therefore, the release of CO_2 seems to be more strongly associated with the formation of Fe_3O_4 nanocrystals as the Fe_3O_4 conversion rate climbs to 93.3% during this stage, which further implies that the Fe_3O_4 nanocrystals may grow via the surface condensation reactions with the precursor fragments (monomer) by releasing CO_2.

In brief, as the small molecules are heavily released during the growth of the Fe_3O_4 nanocrystals, it is reasonable to believe that the pyrolysis of the Fe precursor is strongly associated with the particle growth process.

Impact of Gelification on the Growth Kinetics of Fe_3O_4 Nanocrystals. All above-mentioned results and discussion disclose that the first gelification process exerts a strong impact on the equilibrium size of the Fe_3O_4 nanocrystals by altering the coordination situation of $Fe(acac)_3$, which thus offers an excellent system for further investigating the impact of the pyrolysis behavior of metal precursors on the growth kinetics of nanocrystals.

As a matter of fact, the results shown in Figure 2 also reveal that the particle size distribution (RSD) dramatically decreases, exhibiting a size focusing effect, before the particle reaches its equilibrium size at 30 min of reflux. Meanwhile, the conversion rate increases dramatically from 15 to 30 min of reflux reaching 93.3%, quite close to the maximum conversion rate achieved after 60 min of reflux. Because the aliquots extracted at 0 and 10 min of reflux became gels at room temperature, the method for purifying the nanocrystals exacted later on is not effective for separating the nanocrystals from the unreacted gel-like precursor, quite probably because the fragments of the breakdown molecular network formed by HOOC−PEG−COOH and $Fe(acac)_3$ remain covalently attached on the nanocrystal surface. Consequently, the conversion rates for these two samples are over-rated. Nevertheless, the rest of the conversion rate data, together with temporal evolutions of size and size distribution shown in Figures 2, 6, and 7, already provide sufficient information for understanding the growth behavior of the Fe_3O_4 nanocrystals influenced by the gelification process of the reaction system.

With respect to nanocrystal growth, the size focusing effect and size defocusing effect are widely observed and interpreted by the diffusion-controlled growth model and the surface reaction-controlled growth model in the literature.[3,22,23,26] In the diffusion-controlled growth theory, the particle growth is supposed to be determined by diffusion of monomers to particle surface.[25−27] It is assumed that the average distance between the particles is large enough and the diffusion layer at the periphery of each particle is undisturbed, so that the growth of each particle is independent.[22,25,28] The monomers diffuse from the bulk solution to the particle surface through the diffusion layer and are typically treated in the literature by Fick's First Law given as:[3]

$$J = 4\pi x^2 D\frac{dC}{dx} \quad (1)$$

where J is the flux of monomers passing through a spherical plane with a radius of x, which is the distance from a certain point within the diffusion layer to the center of the particle, D is the diffusion coefficient of monomers, and C is the concentration of monomer.

According to Fick's First Law, J is a constant regardless of x; integrating $C(x)$ from $r + \delta$ to r with respect to x gives eq 2:

$$J = \frac{4\pi Dr(r + \delta)}{\delta}(C_b - C_i) \quad (2)$$

where δ is the thickness of the diffusion layer, C_b is the monomer concentration in bulk solution, and C_i is the monomer concentration at the particle surface.

If the monomers reaching the particle surface are completely consumed by the particle growth, the particle growth rate can be written as a function of J:

$$\frac{dr}{dt} = \frac{V_m J}{4\pi r^2} \quad (3)$$

where V_m is the molar volume of monomer. Combining eqs 2 and 3 gives

$$\frac{dr}{dt} = \frac{DV_m}{r}\left(1 + \frac{r}{\delta}\right)(C_b - C_i) \quad (4)$$

If $r/\delta \ll 1$, the growth rate can be rewritten as[3]

$$\frac{dr}{dt} = \frac{DV_m}{r}(C_b - C_i) \quad (5)$$

Equation 5 lays the theoretical foundation for the diffusion-controlled growth model, according to which the growth rate is proportional to the monomer concentration gradient and inversely proportional to the particle radius. When the concentration gradient is positive, the growth rate is inversely proportional to particle size, which means that the growth of larger particles is retarded while the growth of smaller ones is hastened, leading to size focusing behavior. When the concentration gradient is negative, the growth rate is negative. Smaller particles dissolve into monomers faster than larger ones, resulting in the size defocusing.

With respect to reaction-controlled growth model, it is assumed that the formation of nanocrystals is determined not only by the monomer diffusion process, but also by the surface reaction process. Thus, the particle growth rate is expressed as[22]

$$\frac{dr}{dt} = V_m D C^0_{flat}\left\{\frac{S - \exp\left(\frac{2\gamma V_m}{rRT}\right)}{r + \frac{D}{k^{flat}_g}\exp\left[\alpha\frac{2\gamma V_m}{rRT}\right]}\right\} \quad (6)$$

where S is the supersaturation degree, which can be expressed by $S = C_b/C^0_{flat}$; C^0_{flat} is the solubility of the monomer in equilibrium with bulk material; k^{flat}_g is the surface reaction rate constant for the growth of the corresponding bulk material; γ is the surface free energy per unit area; α is the transfer coefficient for the precipitation and dissolution reaction. When $D \gg k^{flat}_g$, the particle growth follows the surface reaction-controlled model, and the particle growth rate is then written as

$$\frac{dr}{dt} = V_m k^{flat}_g C^0_{flat}\left\{S\exp\left[-\alpha\frac{2\gamma V_m}{rRT}\right] - \exp\left[(1-\alpha)\frac{2\gamma V_m}{rRT}\right]\right\} \quad (7)$$

Following eq 7, it can be seen that the growth rate increases with the radius of the particle, r, which means that large particles show higher growth rate than small particles do. Therefore, if the surface reaction-controlled growth is dominant, the particle size distribution tends to be broadened against reaction time.[22,23,28]

Both the diffusion-controlled growth model and the surface reaction-controlled model are widely used for simulating the growth behavior of inorganic nanocrystals. Nevertheless, the ensemble behavior of the nanocrystals generated upon simple precipitation reactions occurring in aqueous system is better simulated than that for the nanocrystals prepared through the pyrolysis of organic precursors upon the thermal decomposition method.[8,22,28,51] In the latter approach, apart from the diffusion of monomer to nuclei surface and the following surface reactions, the supply of monomer via the pyrolysis of precursors should also be taken into consideration as it strongly influences the particle growth.

Recently, Bawendi and co-workers developed a new theoretical model by taking the thermal decomposition of precursor as the rate-determining step for the particle growth.[29] The decomposition reaction is described by an irreversible reaction given as:

$$P \xrightarrow{k_f} C_1 \quad (8)$$

where k_f is the rate constant for the precursor decomposition, while P and C_1 stand for the precursor and monomers, respectively. The release of small molecules during the pyrolysis of metal precursors $Fe(acac)_3$ supports that the decomposition reaction of metal precursor is hardly reversible.[34,50,52]

On the basis of the reliable reaction conversion rates and TEM sizes, the concentration of the resultant Fe_3O_4 nanocrystals obtained at 15 and 30 min of reflux, as shown in Figures 1 and 2, was calculated to be 1.50×10^{-6} and 1.45×10^{-6} mol/L, respectively. This allows us to assume that the growth of the Fe_3O_4 nanocrystals is based on the reactions between monomers and particles instead of interparticle coagulation; thus the growth and dissociation reaction for n-sized particles can also be written as[29]

$$C_n + C_1 \underset{D_{n+1}}{\overset{G_n}{\rightleftharpoons}} C_{n+1} \quad (9)$$

where G_n and D_n are the time-dependent growth and dissociation frequency of monomer attachment and detachment, respectively.

According to Bawendi's model, the growth rate is assumed to be proportional to both the number of available sites on the particles surface and the concentration of the monomers, and meanwhile the particle dissociation rate is proportional to the number of sites occupied by ligands. The total number of particles binding sites is proportional to the 2/3 power of the monomer number within the particles, based on the hypothesis that the particle is spherical and the unbound ligand concentration is constant. The growth rate and the dissociation rate are then written as follows:

$$G_n = k_a n^{2/3} C_1 \quad (10)$$

$$D_n = k_d n^{2/3} \quad (11)$$

where k_a and k_d are the effective rate constants including the intrinsic rates of monomer addition and dissociation, respectively.[29] The rate equations of precursor, monomer, and n-sized nanocrystal are written as follows:

$$\frac{dP}{dt} = -k_f P \quad (12)$$

$$\frac{dC_1}{dt} = k_f P - k_a C_1^2 - k_a \sum_{n=1}^{N-1}(n)^{2/3} C_n C_1 + k_d (2)^{2/3} C_2 + k_d \sum_{n=2}^{N}(n)^{2/3} C_n \quad (13)$$

$$\frac{dC_n}{dt} = k_a (n-1)^{2/3} C_{n-1} C_1 - k_d (n)^{2/3} C_n - k_a (n)^{2/3} C_n C_1 + k_d (n+1)^{2/3} C_{n+1} \quad (14)$$

where N is the maximum number of monomers in particle. Two parameters were extracted by Bawendi and co-workers for

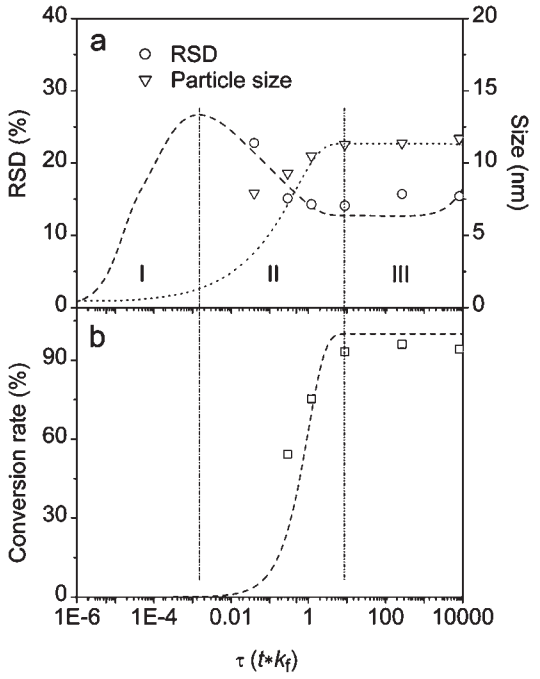

Figure 12. The best simulation results on particle size (- - -), size distribution (RSD, — — —) in frame a, and conversion rate of Fe precursor in frame b, overlaid with the corresponding experimental data shown in Figure 2. The parameter values for α and β are 1.0×10^9 and 2.0×10^0, respectively. The conversion rates for particles obtained at reflux times of 0 and 10 min were abandoned as they were overestimated.

further analyzing the particle growth via the nondimensional processing of eqs 12−14, that is:

$$\alpha = \frac{k_a P_0}{k_f} \tag{15}$$

$$\beta = \frac{k_d}{k_f} \tag{16}$$

where P_0 is the initial precursor concentration. These two nondimensional parameters, α and β, correspond to scaled growth and dissociation rates, respectively.

Following the method described by Bawendi and co-workers, the nondimensionalized expressions of eqs 12−14 given as eqs S1−3 in the Supporting Information were integrated using the continuous Fokker−Planck partial differential equation, and the following experimental quantities were computed on the basis of the concentration equations including the mean size (D), radial variance (σ_R^2), relative standard deviation (RSD), and reaction conversion rate (Y). More details on the simulation method and parameters are provided in the Supporting Information.

The best simulation results on size, size distribution, and conversion rate presented in Figure 2 are shown in Figure 12 with α and β corresponding to 1.0×10^9 and 2.0×10^0, respectively. According to the simulation results, the growth process of Fe_3O_4 nanocrystals can be divided into three distinct regions. In the first region, the conversion rate of precursor is very low, and the size and size distribution are mainly determined by the nucleation process. In the second region, that is, the growth stage, the particle size increases with the conversion rate of precursor; meanwhile, the size distribution is reduced. In the third region, the particle growth nearly stops, while the conversion rate of

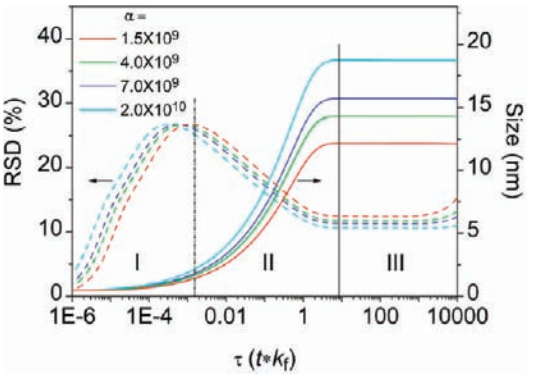

Figure 13. The best simulation results on particle size and size distribution for the Fe_3O_4 nanocrystals (shown in Figure 7) obtained by aging the stock solution at 40 °C for 12 h (red lines, 12.1 nm), at 40 °C for 72 h (green lines, 14.1 nm), at 80 °C for 4 h (blue lines, 15.6 nm), and at 140 °C for 4 h (cyan lines, 18.9 nm), respectively. The parameter value of β is fixed as 2.0×10^0.

precursor reaches 100%. Meanwhile, the size distribution remains nearly constant for some time, and then slightly increases upon further reaction. It was demonstrated that the variation of RSD in the third region is dependent on the value initially set for β. As shown in Figure S7, further decreasing β simply flattens the tail of the RSD curve without changing the equilibrium size achieved at the end of the second region. In general, the simulation results match well with the experimental results shown in Figure 2, and the size focusing effect is also well depicted with respect to the Fe_3O_4 nanocrystals synthesized without purposely imposing a preaging process for increasing the gelification degree.

As decreasing β does not change the simulation results on the equilibrium size and the corresponding RSD at the end of the particle growth stage as shown in Figure S7, β was fixed in the following simulations on the particle size and size distributions of those Fe_3O_4 nanocrystals shown in Figure 7 for further understanding the impact of gelification on the growth as well as the equilibrium size of Fe_3O_4 nanocrystals eventually achieved. On the basis of the best fits shown in Figure 13, a series of α values was extracted as 1.5×10^9, 4.0×10^9, 7.0×10^9, and 2.0×10^{10} for 12.1, 14.1, 15.6, and 18.9 nm Fe_3O_4 nanocrystals, respectively.

In the expression of α, that is, k_aP_0/k_f, P_0 was fixed during the experiments and k_a should remain unchanged as it represents the rate constant for the monomer addition on particle surface. Consequently, α is inversely proportional to k_f that represents the rate constant for the precursor decomposition. Therefore, it can be concluded that the increased equilibrium size, in consequence of the increased gelification degree of the stock solution, is intrinsically caused by the reduced decomposition rate constant of the precursors, which involves HOOC−PEG−COOH in forming a large molecular network.

To further verify the above conclusion, the growth of Fe_3O_4 nanocrystals formed in the nongelification system containing mPEG−COOH (Figure 10) was also simulated with the best results being shown in Figure S8. The value of α extracted was in the magnitude of 10^6, which is greatly smaller than those extracted from the gelification systems, even though $Fe(acac)_3$ was used in all of these systems as the starting material. The reduced α as a result of the increased rate constant for precursor decomposition is greatly in favor of burst of nuclei; consequently, the equilibrium size of the Fe_3O_4 nanocrystals is much smaller in

the nongelification system and also reached more quickly. In this context, it is easy to understand why the as-prepared iron oxide nanocrystals are typically of several nanometers in diameter by using $Fe(acac)_3$ as precursor except for those prepared via the seed-mediated growth,[7,20,31,35,53,54] because the rate constant k_f for the precursor decomposition is determined by the chemical nature of the precursor.

CONCLUSIONS

In summary, nearly monodispersed Fe_3O_4 nanocrystals with the diameter ranging from 5.8 to 18.9 nm were synthesized in diphenyl oxide by the thermal decomposition method through a single preparation recipe comprised of $Fe(acac)_3$, HOOC−PEG−COOH, and oleylamine. Systematic experiments reveal that HOOC−PEG−COOH used for the biocompatible surface coating can cross-link $Fe(acac)_3$ molecules with the aid of oleylamine to form gels. Further investigations demonstrate that the gelification degree is strongly associated with the equilibrium size of the resultant Fe_3O_4 nanocrystals. Simply by manipulating the gelification degree through aging the stock solutions with the same preparation recipe, the equilibrium size of the Fe_3O_4 nanocrystals has effectively been tuned over a size range of 11.3−18.9 nm. The PES/PIMS analysis on the small molecules released during the reaction suggests that the nanocrystal growth is strongly correlated to the pyrolysis reactions taking place in the reaction system. Theoretical analysis and numerical simulations on the particle growth behavior suggest that the complexation between HOOC−PEG−COOH and $Fe(acac)_3$, apparently inducing the gelification of the reaction system, intrinsically reduces the thermal decomposition rate constants of the Fe precursors in the new forms, and eventually gives rise to the gelification-associated size regulation effect for Fe_3O_4 nanocrystals by altering their growth kinetics.

The delicate control over the particle size is not only meaningful for discovering the particle size-related physical properties of inorganic nanocrystals, but also important for further achieving advanced nanomaterials with well-defined properties. The current investigations have demonstrated that the gelification of the reaction system can be used as an effective measure for tuning the size of resultant nanocrystals. Although the gelification phenomenon does not always occur in the thermal decomposition systems for producing high-quality nanocrystals, the underlying principle can be adopted for effectively regulating the size of nanocrystals by manipulating the complexation between metal precursor and organic ligands or additives.

ASSOCIATED CONTENT

Supporting Information. (1) TGA curve of the 11.3 nm Fe_3O_4 nanoparticles, (2) hydrodynamic size distribution profiles of Fe_3O_4 particles obtained at different reflux times, (3) TEM image of Fe_3O_4 nanoparticles extracted at around 224 °C during the heating process, (4) absorption spectra of $Fe(acac)_3$, oleylamine, and HOOC−PEG−COOH, (5) TEM image of Fe_3O_4 nanoparticles obtained by 2 h of reflux in the absence of oleylamine, (6) typical photoelectron spectra of the small molecules released during the preparation, (7) the simulation results on the particle size and size distribution obtained by using different β values based on a fixed α value, and (8) the best simulation results on particle size and size distribution, overlaid with the corresponding experimental data extracted from Figure 10; along with the expressions of simulated quantities, method, and parameters. This material is available free of charge via the Internet at http://pubs.acs.org.

AUTHOR INFORMATION

Corresponding Author
gaomy@iccas.ac.cn; fenglonggu@gmail.com

ACKNOWLEDGMENT

We thank the National Basic Research Program of China (2011CB935800), NSFC (81090271, 21003135, 20820102035, 21021003), and CAS (KJCX2-YW-M15) for financial support. Q. J. also is grateful to Prof. Maofa Ge and Prof. Jun Zhang for their kind help with respect to PES/PIMS and viscosity experiments.

REFERENCES

(1) Alivisatos, A. P. *Science* **1996**, *271*, 933.
(2) Roca, A. G.; Costo, R.; Rebolledo, A. F.; Veintemillas-Verdaguer, S.; Tartaj, P.; Gonzalez-Carreno, T.; Morales, M. P.; Serna, C. J. *J. Phys. D: Appl. Phys.* **2009**, *42*, 224002.
(3) Sugimoto, T. *Monodispersed Particles*, 1st ed.; Elsevier: Amsterdam, 2001; pp 368−376.
(4) Pradhan, N.; Reifsnyder, D.; Xie, R. G.; Aldana, J.; Peng, X. G. *J. Am. Chem. Soc.* **2007**, *129*, 9500.
(5) Yu, W. W.; Wang, Y. A.; Peng, X. G. *Chem. Mater.* **2003**, *15*, 4300.
(6) Park, J.; An, K. J.; Hwang, Y. S.; Park, J. G.; Noh, H. J.; Kim, J. Y.; Park, J. H.; Hwang, N. M.; Hyeon, T. *Nat. Mater.* **2004**, *3*, 891.
(7) Sun, S. H.; Zeng, H. *J. Am. Chem. Soc.* **2002**, *124*, 8204.
(8) Murray, C. B.; Norris, D. J.; Bawendi, M. G. *J. Am. Chem. Soc.* **1993**, *115*, 8706.
(9) Ahrenstorf, K.; Heller, H.; Kornowski, A.; Broekaert, J. A. C.; Weller, H. *Adv. Funct. Mater.* **2008**, *18*, 3850.
(10) Rockenberger, J.; Scher, E. C.; Alivisatos, A. P. *J. Am. Chem. Soc.* **1999**, *121*, 11595.
(11) Hyeon, T.; Lee, S. S.; Park, J.; Chung, Y.; Na, H. B. *J. Am. Chem. Soc.* **2001**, *123*, 12798.
(12) Park, J.; Lee, E.; Hwang, N. M.; Kang, M. S.; Kim, S. C.; Hwang, Y.; Park, J. G.; Noh, H. J.; Kini, J. Y.; Park, J. H.; Hyeon, T. *Angew. Chem., Int. Ed.* **2005**, *44*, 2872.
(13) Sun, S. H.; Zeng, H.; Robinson, D. B.; Raoux, S.; Rice, P. M.; Wang, S. X.; Li, G. X. *J. Am. Chem. Soc.* **2004**, *126*, 273.
(14) Jana, N. R.; Chen, Y. F.; Peng, X. G. *Chem. Mater.* **2004**, *16*, 3931.
(15) Casula, M. F.; Jun, Y. W.; Zaziski, D. J.; Chan, E. M.; Corrias, A.; Alivisatos, A. P. *J. Am. Chem. Soc.* **2006**, *128*, 1675.
(16) Yu, W. W.; Falkner, J. C.; Yavuz, C. T.; Colvin, V. L. *Chem. Commun.* **2004**, 2306.
(17) Si, R.; Zhang, Y. W.; Zhou, H. P.; Sun, L. D.; Yan, C. H. *Chem. Mater.* **2007**, *19*, 18.
(18) Cheon, J. W.; Kang, N. J.; Lee, S. M.; Lee, J. H.; Yoon, J. H.; Oh, S. J. *J. Am. Chem. Soc.* **2004**, *126*, 1950.
(19) Woo, K.; Hong, J.; Choi, S.; Lee, H. W.; Ahn, J. P.; Kim, C. S.; Lee, S. W. *Chem. Mater.* **2004**, *16*, 2814.
(20) Xu, Z.; Shen, C.; Hou, Y.; Gao, H.; Sun, S. *Chem. Mater.* **2009**, *21*, 1778.
(21) Sugimoto, T. *Adv. Colloid Interface Sci.* **1987**, *28*, 65.
(22) Talapin, D. V.; Rogach, A. L.; Haase, M.; Weller, H. *J. Phys. Chem. B* **2001**, *105*, 12278.
(23) van Embden, J.; Sader, J. E.; Davidson, M.; Mulvaney, P. *J. Phys. Chem. C* **2009**, *113*, 16342.
(24) Lifshitz, I. M.; Slyozov, V. V. *J. Phys. Chem. Solids* **1961**, *19*, 35.
(25) Reiss, H. *J. Chem. Phys.* **1951**, *19*, 482.
(26) Peng, X. G.; Wickham, J.; Alivisatos, A. P. *J. Am. Chem. Soc.* **1998**, *120*, 5343.

(27) Lamer, V. K.; Dinegar, R. H. *J. Am. Chem. Soc.* **1950**, *72*, 4847.
(28) Park, J.; Joo, J.; Kwon, S. G.; Jang, Y.; Hyeon, T. *Angew. Chem., Int. Ed.* **2007**, *46*, 4630.
(29) Rempel, J. Y.; Bawendi, M. G.; Jensen, K. F. *J. Am. Chem. Soc.* **2009**, *131*, 4479.
(30) Han, W.; Yi, L. X.; Zhao, N.; Tang, A. W.; Gao, M. Y.; Tang, Z. Y. *J. Am. Chem. Soc.* **2008**, *130*, 13152.
(31) Lu, X. Y.; Niu, M.; Qiao, R. R.; Gao, M. Y. *J. Phys. Chem. B* **2008**, *112*, 14390.
(32) Hu, F. Q.; Li, Z.; Tu, C. F.; Gao, M. Y. *J. Colloid Interface Sci.* **2007**, *311*, 469.
(33) Li, Z.; Wei, L.; Gao, M. Y.; Lei, H. *Adv. Mater.* **2005**, *17*, 1001.
(34) Li, Z.; Sun, Q.; Gao, M. Y. *Angew. Chem., Int. Ed.* **2005**, *44*, 123.
(35) Li, Z.; Chen, H.; Bao, H. B.; Gao, M. Y. *Chem. Mater.* **2004**, *16*, 1391.
(36) Hu, F. Q.; Wei, L.; Zhou, Z.; Ran, Y. L.; Li, Z.; Gao, M. Y. *Adv. Mater.* **2006**, *18*, 2553.
(37) Liu, S. J.; Jia, B.; Qiao, R. R.; Yang, Z.; Yu, Z. L.; Liu, Z. F.; Liu, K.; Shi, J. Y.; Han, O. Y.; Wang, F.; Gao, M. Y. *Mol. Pharmaceutics* **2009**, *6*, 1074.
(38) Liu, S. J.; Han, Y. C.; Qiao, R. R.; Zeng, J. F.; Jia, Q. J.; Wang, Y. L.; Gao, M. Y. *J. Phys. Chem. C* **2010**, *114*, 21270.
(39) Yao, L.; Zeng, X.; Ge, M.; Wang, W.; Sun, Z.; Du, L.; Wang, D. *Eur. J. Inorg. Chem.* **2006**, *2006*, 2469.
(40) Xing, B.; Yu, C.-W.; Chow, K.-H.; Ho, P.-L.; Fu, D.; Xu, B. *J. Am. Chem. Soc.* **2002**, *124*, 14846.
(41) Lesnyak, V.; Voitekhovich, S. V.; Gaponik, P. N.; Gaponik, N.; Eychmüller, A. *Acs Nano* **2010**, *4*, 4090.
(42) Barnum, D. W. *J. Inorg. Nucl. Chem.* **1961**, *21*, 221.
(43) Roggeman, E. J.; Scurto, A. M.; Brennecke, J. F. *Ind. Eng. Chem. Res.* **2000**, *40*, 980.
(44) Holm, R. H.; Cotton, F. A. *J. Am. Chem. Soc.* **1958**, *80*, 5658.
(45) Nakamoto, K. *Infrared and Raman Spectra of Inorganic and Coordination Compounds*; John Wiley & Sons, Ltd.: Hoboken, 2009.
(46) Electrolytes, Electromotive Force, and Chemical Equilibrum. In *Lange's Handbook of Chemistry*, 15th ed.; Dean, J. A., Ed.; McGraw-Hill, Inc.: New York, 1999.
(47) Ismail, H. M. *J. Anal. Appl. Pyrolysis* **1991**, *21*, 315.
(48) Kimura, K.; Achiba, Y.; Yamazaki, T.; Iwata, S. *Handbook of HeI Photoelectron Spectra of Fundamental Organic Molecules*; Japan Scientific Societies: Tokyo, 1981.
(49) Vonhoene, J.; Charles, R. G.; Hickam, W. M. *J. Phys. Chem.* **1958**, *62*, 1098.
(50) Tu, C. F.; Du, J. J.; Yao, L.; Yang, C. H.; Ge, M. F.; Xu, C. L.; Gao, M. Y. *J. Mater. Chem.* **2009**, *19*, 1245.
(51) Rao, C. N. R.; Varghese, N.; Biswas, K. *Chem.-Asian J.* **2008**, *3*, 1435.
(52) Kwon, S. G.; Piao, Y.; Park, J.; Angappane, S.; Jo, Y.; Hwang, N. M.; Park, J. G.; Hyeon, T. *J. Am. Chem. Soc.* **2007**, *129*, 12571.
(53) Jun, Y. W.; Huh, Y. M.; Choi, J. S.; Lee, J. H.; Song, H. T.; Kim, S.; Yoon, S.; Kim, K. S.; Shin, J. S.; Suh, J. S.; Cheon, J. *J. Am. Chem. Soc.* **2005**, *127*, 5732.
(54) Lee, J. H.; Huh, Y. M.; Jun, Y.; Seo, J.; Jang, J.; Song, H. T.; Kim, S.; Cho, E. J.; Yoon, H. G.; Suh, J. S.; Cheon, J. *Nat. Med.* **2007**, *13*, 95.